Spectral Phase Measurements of Heterodyne Detection in Interfacial Broadband Electronic Spectroscopy

Tong Zhang[1,2,3], Zhichao Huangfu[3], Yuqin Qian[3], Zhou Lu[4*], Hong Gao[1*], and Yi Rao[3*]

[1]Beijing National Laboratory for Molecular Sciences and State Key Laboratory of Molecular Reaction Dynamics, Institute of Chemistry, Chinese Academy of Sciences, Beijing 100190, China

[2]University of Chinese Academy of Sciences, Beijing 100049, China

[3]Department of Chemistry and Biochemistry, Utah State University, Logan, UT 84322

[4]Anhui Province Key Laboratory of Optoelectronic Material Science and Technology, School of Physics of Electronic Information, Anhui Normal University, Wuhu, Anhui, China 241002

Abstract

Spectral phase is vital to retrieve both the real and imaginary parts of both second-order vibrational and electronic sum frequency generation spectra. Despite recent efforts, phase measurements in electronic spectra at interfaces are lacking. In particular, references are not well established for frequency-dependent spectral phases in interfacial electronic spectroscopy. In this work, we present broadband heterodyne detection (HD) of interfacial electronic spectroscopy for spectral phases of references. Such a broadband HD method was based upon a broadband short-wave IR laser source from 1100 to 2200 nm. A collinear geometry was adopted for passive phase stability. We further compared often-used reference samples, including gold (Au) thin films, silver (Ag) thin films, *p*-type GaP (100), *p*-type GaAs (100), as well as left-handed and right-handed z-cut α-quartz crystals. The phases of the second order susceptibilities for Ag thin films, the GaP crystal, the GaAs crystal, and the quartz crystals are independent of frequency from 630 to 730 nm. More importantly, it was found that the often-used Au thin film in the literature is not a good phase reference for frequency-dependent phases.

Corresponding authors: Yi Rao (yi.rao@usu.edu), Zhou Lu (zhoulu@ahnu.edu.cn), and Hong Gao (honggao2017@iccas.ac.cn)

Introduction

Second-order nonlinear spectroscopies have evolved into analytical tools for surfaces and interfaces since the 1980s.[1-13] Both vibrational and electronic sum frequency generation spectroscopies hold the central focus in this field are the main players of the second-order spectroscopies.[1-43] The former is so-called VSFG and the latter ESFG. The interface-specific electronic and vibrational spectra are often collected in a form of frequency-dependent intensity. It turns out that phase information is often hidden in an intensity spectrum of VSFG or ESFG. The spectral phase of a material, $\phi(\omega)$, is correlated with linear and nonlinear frequency-dependent responses with light. In second order nonlinear optical spectroscopy, the spectral phase enables one to retrieve both the real and imaginary parts of a spectrum, leading to the purely absorptive spectra for peak identifications of interfacial molecules with frequency-dependent dispersion components. Such frequency-dependent phase information is intrinsically manifested in the macroscopic susceptibility, $\chi^{(2)}(\omega)$, for materials at interfaces, or the microscopic hyperpolarizability, $\beta^{(2)}(\omega)$, for crystals, molecules, or chemical groups at interfaces.[44-46] Previous studies showed the advantages of phase measurements: 1) Extraction of the absolute orientation of molecules;[45] 2)Isolation of a signal produced by a specific interface in a layered sample with a well-defined phase reference;[47] 3) Deconvolution of surface from bulk responses of nonlinear signals with an absolute phase;[48] 4) Separation of pathways for multiple transitions,[49] etc.

Phase-sensitive VSFG measurements were first implemented by Shen and co-workers.[44, 50] Recently, heterodyne detection (HD) for spectral phases in broadband VSFG was demonstrated by Benderskii et al,[51] followed by many other groups.[52-67] On the other hand, phase measurements in interfacial electronic spectra have been performed by Eisenthal and co-workers.[68] Lately, HD for spectral phases in broadband interfacial electronic spectra was demonstrated by Tahara et al,[45] and Roberts et al.[47] As compared with those in vibrational SFG spectra, phase measurements in electronic spectra at interfaces are often neglected.

Originally, phase modulation was the main approach for extracting spectral phase of $\chi^{(2)}(\omega)$ or $\beta^{(2)}(\omega)$ in interfacial electronic spectra.[44, 50, 69-72] Such a method requires a phase modulator to change its length or refractive index. It turned out that the phase modulation method was time-consuming due to mechanical errors from moving optical elements. It is noteworthy that Wang and coworkers reported an elegant phase measurement with a well-defined α-quartz as an internal

standard for interferemetry.[73] Such an idea was later extended with a delicate design of a Michelson interferometer by Shultz et al.[57, 58, 74] Recently, the HD method received increasing attention from phase measurements in ESFG and second harmonic generation (SHG) experiments with the advanced femtosecond broadband lasers.[45, 47, 75-77] The HD was based upon spectral interferometry (SI) by measuring interference between weak optical signal and a time-delayed local oscillator (LO) in frequency domain.[78] Furthermore, the LO introduced in the HD experiments enables one to improve detection sensitivity and fast measurements, even without significant signal-to-noise consequences. Nevertheless, the challenging part of the HD-ESFG is to seek a LO, which has a spectrum broad enough to cover spectral range of signals of interest. Previous successes in HD-ESFG were based upon the generation of a LO before or after samples by mixing two different visible beams.[45] In fact, one could use a broadband laser beam to achieve the same goal. Heterodyne second harmonic generation (HD-SHG) was a complementary method for phase measurements in interfacial electronic spectroscopy.[72, 79-83] However, these HD experiments were limited to a narrow band of ca. 200 cm^{-1} for spectral purposes.

In this work, we present an alternative approach to determine spectral phases by combining heterodyne detection interfacial electronic spectroscopy (HD-iES) with broadband SHG (*b*-SHG). We further established phase references for interfacial electronic spectroscopy. Six often-used phase references, including left-handed and right-handed α-quartz crystals, Au, Ag, *p*-type GaP (100), and *p*-type GaAs (100) were examined in an effort to search for the best choice of phase references in interfacial second-order spectroscopy.

Theoretical consideration

We shall start with a general formula to describe phase measurements. Interference intensity from any second-order signal of interest and a LO takes the form of,

$$I(\omega,\tau,\phi_M) \propto \left| \int_{-\infty}^{+\infty} dt\left[E_i(t) + E_{LO}(t-\tau)e^{-i\phi_M}\right]e^{-i\omega t} \right|^2$$
$$= \left|E_i(\omega) + E_{LO}(\omega)e^{-i\phi_M + i\omega\tau}\right|^2 \quad (1)$$

where τ is the time delay between the signal, $E_i(t)$ and the LO, $E_{LO}(t-\tau)$, and ϕ_M is the phase with modulations. In the case of second-order responses, SFG (ω) is generated by two incident beams (ω_1 and ω_2). The SFG electric field is expressed as,[84]

$$E(\omega) = \frac{i\omega}{n(\omega)c}\chi^{(2)}(\omega)E(\omega_1)E(\omega_2) \quad (2)$$

where $n(\omega)$ is the frequency-dependent refractive index for SFG and c the speed of light.

Equation 1 is further simplified as

$$I(\omega,\tau,\phi_M) \propto \left|\chi^{(2)}{}_i(\omega) + \chi^{(2)}{}_{LO}(\omega)e^{-i\phi_M+i\omega\tau}\right|^2$$
$$= |\chi^{(2)}{}_i(\omega)|^2 + |\chi^{(2)}{}_{LO}(\omega)|^2 + 2|\chi^{(2)}{}_i(\omega)\chi^{(2)}{}_{LO}(\omega)|cos\,(\phi_i(\omega) - \phi_{LO}(\omega) - \phi_M(\omega) + \omega\tau + \phi_0) \quad (3)$$

where $\phi_i(\omega)$ and $\phi_{LO}(\omega)$ are the phases of the second-order electric fields from the samples and the LO, respectively, and ϕ_0 is the phase due to the difference of electric fields for the samples and the LO. It is seen from Equation 3 that the phase factor of $\omega\tau$ causes SFG oscillations as a function of ω. However, we are more interested in $\phi_i(\omega)$ of $\chi^{(2)}{}_i(\omega)$ from interfaces. In Equation 1, the first two terms are often called the "direct current" (DC) part while the last oscillatory term is called the "alternate current" (AC) part. Thus, one is able to obtain intensity interference from varying $\phi_M(\omega)$ (phase modulation) or direct spectral modulation with $\omega\tau$ (spectral interferometry). The former is called phase modulation detection, while the latter is so-called heterodyne detection.

The phase modulation yields interference second-order signals when the time delay, τ, is set to be zero. Equation 3 is rewritten as,

$$I(\omega,\Phi_M) \propto \left|\chi^{(2)}{}_i(\omega)\right|^2 + \left|\chi^{(2)}{}_{LO}(\omega)\right|^2 + 2|\chi^{(2)}{}_i(\omega)\chi^{(2)}{}_{LO}(\omega)|\,cos(\phi_i(\omega) - \phi_{LO}(\omega) - \Phi_M(\omega) + \phi_0)$$

$$= |\chi^{(2)}{}_i(\omega)|^2 + |\chi^{(2)}{}_{LO}(\omega)|^2 + 2|\chi^{(2)}{}_i(\omega)\chi^{(2)}{}_{LO}(\omega)|cos\,(\phi_i(\omega) - \phi_{LO}(\omega) - \Delta k(\omega)l + \phi_0) \quad (4)$$

where $\Delta k(\omega)$ is the wave-vector mismatch, and l is the distance that a LO and incident beams travel through a phase modulator, and ϕ_0 the phase difference due to the propagation of the fundamental lights on a sample and a LO. The phase modulation is often achieved by varying either $\Delta k(\omega)$ or l.

On the other hand, heterodyne detection measures interference fringes in frequency domain when $\Delta k(\omega)l$ is set to be zero or constant. Equation 3 is further simplified as,[78]

$$I(\omega,\tau) \propto \left|\chi^{(2)}{}_i(\omega)\right|^2 + \left|\chi^{(2)}{}_{LO}(\omega)\right|^2 + 2\left|\chi^{(2)}{}_i(\omega)\chi^{(2)}{}_{LO}(\omega)\right| cos\,(\phi_i(\omega) - \phi_{LO}(\omega) + \omega\tau + \phi_0) \quad (5)$$

A routine treatment of Fourier analysis for the spectral interferometry yields the phase $\phi_i(\omega) - \phi_{LO}(\omega) + \omega\tau + \phi_0$ in Equation 5. To obtain the spectral phase of a sample, $\phi_S(\omega)$, one has to measure a phase from a known reference with the same procedure, $\phi_R - \phi_{LO}(\omega) + \omega\tau + \phi_0$. Subtraction out of $\phi_{LO}(\omega)$, $\omega\tau$, and ϕ_0 produces $\phi_S(\omega) - \phi_R$, thereby yielding the spectral phase of the sample, $\phi_S(\omega)$.

Experimental Methods

Laser Source. A Ti-Sapphire amplifier system (UpteK Solutions) centered at 800 nm with 1 kHz, 4 W, and 100 fs was used for our experiments. A portion of 1.5 mJ was split to generate a short-wave infrared (SWIR) source from a home-built broadband optical parametric amplifier (BOPA). The BOPA was based on a type I BiB_3O_6 (BIBO) crystal. In our early work,[85, 86] we presented a two-stage BOPA for the broadband SWIR source, in which a white light continuum was generated as a seed pulse. The two-stage BOPA caused stability issues due to the non-trivial continuum light. Here we generated a broadband SWIR from 1200 nm to 2200 nm by using a one-stage BOPA without the white light continuum seed. As a result, an ultrabroadband SWIR beam of 160 μJ was generated with a same polarization for both signal (1200-1600 nm) and idler (1600-2200 nm) with a pulse duration of around 200 fs. The pulse duration of the SWIR was measured by mixing an 800 nm (100 fs) with the SWIR and collecting SFG signals from silver thin films, as shown in Figure S1.

Optical layout. We used a periscope to introduce 45° polarized light, followed by a broadband polarizer (Thorlabs) to choose the polarization of the fundamental light. A short-pass filter (1500 nm, Edmund) was placed to remove long-wavelength light and high-order harmonic light generated by the optics along the light path. A one-inch CaF_2 lens with 150 mm focus length (spot size of 130 um) was applied to focus the SWIR fundamental light onto the sample at an angle of 45° with respect to the surface normal. A long-pass filter (1000 nm, Thorlabs) was placed right after the lens. The fundamental light was filtered out by combining three optical filters, including

a 900 nm short-pass filter (Thorlabs), a 445 nm long-pass filter (Thorlabs), and 780 nm short-pass filter (Thorlabs). The ultrabroadband SWIR of 10 μJ was used for our experiments by adjusting neutral density filters. A spectrometer (Kymera 328i-C, Andor Technology) with a thermally-cooled charge-coupled device (CCD) detector (IDus DU420A-BVF, 1024 × 255, Andor Technology) was used for spectral collection.

Heterodyne Detection. Figure 1 (A) displays a schematic setup for broadband HD detection of interfacial electronic spectroscopy. A z-cut α-quartz crystal (MTI Corp.) of 100 μm was used as a LO. A z-cut alpha-quartz crystal is a birefringence crystal with its optical axis perpendicular to the quartz surface. The incident light propagates along the optical axis of the z-cut alpha-quartz. In other words, any rotation around the surface normal does not disrupt the polarization after going through the quartz. The LO was positioned right after the focus lens and the filter. Glass slides were used as time delay generators and placed right after the LO, leading to temporal separation of the LO from *b*-SHG signal. As a result, the LO propagates temporally after the signal due to the positive dispersion. On the other hand, the generated *b*-SHG LO and the transmitted fundamental beam remained spatially collinear when overlapped at interfaces. The usage of the *z*-cut α-quartz crystal ensured that the polarization of the fundamental beam remained the same while the intensity of a LO could be varied with the rotation of the crystal. The time delay between a local oscillator and measured signals dictates spectral interference cycle ($\Delta\nu=1/t$). The larger a time delay, the narrower a spectral interference cycle. For HD-iES, an interfacial electronic spectrum was usually as broad as 500 cm^{-1}, a time delay of 100 – 200 fs was used for accurate phase control.

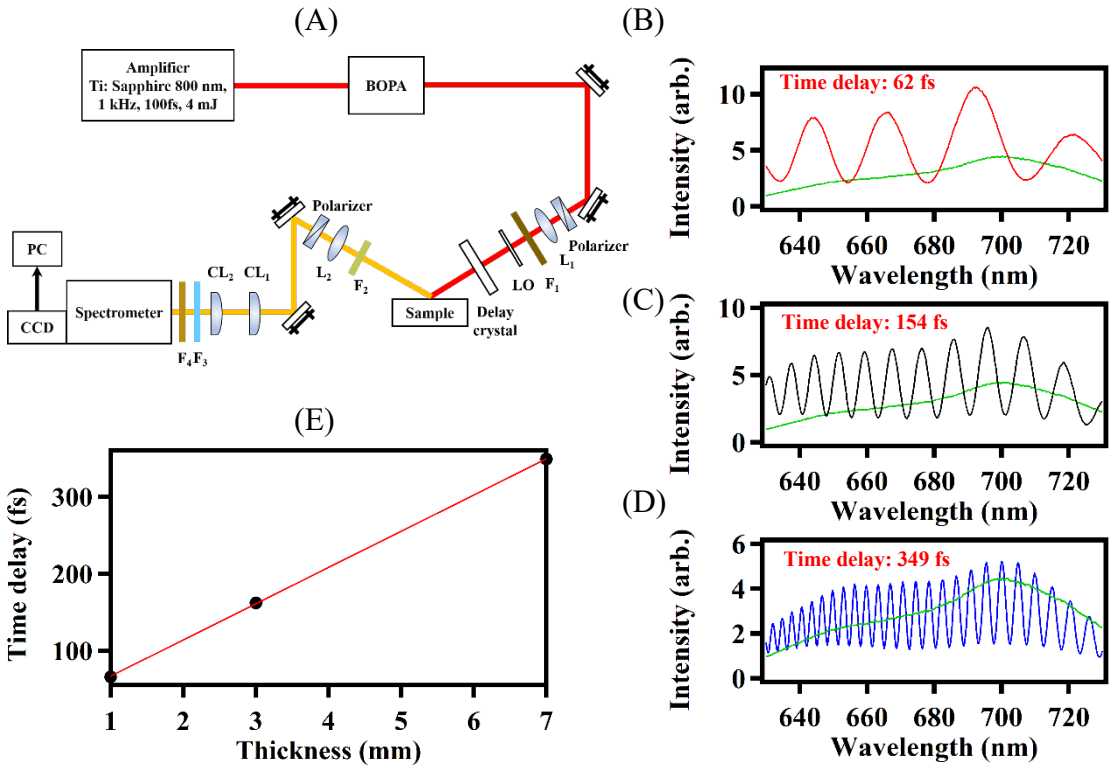

Figure 1. (A) A schematic setup for broadband HD detection of interfacial electronic spectroscopy. (B)-(D) are interference *b*-ESHG spectra from *n*-type GaP (100) along the [0$\bar{1}$1] axis for three different thickness of delay generator glasses (1 mm, 3 mm, and 7 mm). Green lines represent the corresponding LO signals. L_1: 20 cm lens; L_2: 20 cm lens; CL_1: vertically cylindrical lens; CL_2: horizontally cylindrical lens; LO: a local oscillator of z-cut quartz crystal; F_1: 1000 nm long-pass filter; F_2: 900 nm short-pass filter; F_3: 445 nm long-pass filter; F_4: 780 nm short-pass filter. (E) Time delay as a function of thickness for three different delay generator glasses.

Data analysis. A custom Matlab program was used to extract spectral phases from measured interferometry spectra by Fourier filtering. The algorithm for the Fourier filtering was described as follows: 1) Make Jacobian transformation to frequency domain from the wavelength domain measured; 2) Take Discrete inverse Fourier transformation; 3) Use a Cosine window to remove the "DC" part in time domain; 4) Implement discrete Fourier transformation back to frequency domain; 5) Unwrap frequency-dependent angles and convert to wavelength domain.

Samples. Left-handed and right-handed z-cut α-quartz crystals **(**12.5 × 12.5 × 10 mm**)** were purchased from Brightcrystals Technology Inc. *p*-type GaP ((100) orientation, Zn-doped, 4.0-5.2 $\times 10^{17}$ cm^{-3}, 2"×0.45 mm diameter), *n*-type GaP ((100) orientation, S-doped, 2.0-12.0 × 10^{17} cm^{-3}, 5 × 5 × 0.5 mm) and *p*-type ((100) orientation, Zn-doped, 1.3-2.2 × 10^{19} cm^{-3}, 5 × 5 × 0.5 mm) GaAs wafers were purchased from MTI Corporation. Ag thin films (protected silver mirrors, PF10-03-P01) were purchased from Thorlabs. The mirrors were claimed to have a durable SiO_2 overcoat with an approximate thickness of 100 nm. Au thin films were purchased from Platypus Technologies (Partnumber:AU.1000.ALSI). The thickness of the Au thin films was confirmed to be on the order of 100 nm as claimed, with our AFM measurements in Figure S2.

Results

To illustrate our broadband HD-iES experiments, we chose an *n*-type GaP (100) surface as an example to generate *b*-ESHG signals. Figure 1 (B)-(D) show spectral interference of *b*-ESHG from *n*-type GaP (100) along the direction of $[0\bar{1}1]$ for three different delay generators with thicknesses of 1 mm, 3 mm, and 7 mm, respectively. The envelope "DC" signal is readily separated from the oscillatory cross terms by using a traditional Fourier filtering process. Single spectral interference cycles for the three time-delay generators were determined to be 539.1 cm^{-1} (95 points/cycle), 216.2 cm^{-1} (41 points/cycle), and 95.5 cm^{-1} (18 points/cycle). Each spectral point represents a phase of 3.79°, 8.78°, and 20.00°, respectively. Figure 1 (E) shows that the time delay introduced by the three glass windows is proportional to the thickness with a group velocity delay of 41.0 fs/mm at 650 nm and 1300 nm for the glass material as expected. Owing to the collinear geometry, the phase was passively stabilized.

Left-handed and right-handed z-cut α-quartz crystals as standard references. A reference with a known phase is needed to retrieve spectral phases for samples of interest. In particular, an ideal reference is

anticipated to be independent of experimental wavelengths. For this reason, α-quartz crystal is an excellent choice with no absorption in the laser wavelength range from 300 nm to 2400 nm. We calibrated and labeled the +X direction for both left-handed and right-handed z-cut α-quartz crystals by piezoelectric measurements and VSFG methods.[73] The quartz crystals were then positioned as the +X direction was in the incident plane for HD-iES experiments, shown in the insets of Figure 2. Figure 2 shows interference *b*-ESHG spectra of both the left-handed and right-handed z-cut α-quartz crystals, for S-in/P-out (A) and P-in/P-out (B). Both the spectra show the same interference pattern over a large spectral range. The spectral cycles in the two cases are well overlapped, suggesting that both the left-handed and right-handed α-quartz crystals exhibit the same sign. Our results are consistent with that reported in VSFG experiments.[73]

To quantify the phases of z-cut α-quartz crystals for S-in/P-out (SP) and P-in/P-out (PP), the bulk macroscopic susceptibilities, $\chi^{(2)}_{Quartz,B}$, are expressed as,[73]

$$\chi^{(2)}_{Quartz,SP,B}(\omega) = L_{XX}(\omega)L_{YY}(\omega_1)L_{YY}(\omega_1)\cos\alpha_a\beta^{(2)}_{xxx}\cos3\varphi_a$$
$$\chi^{(2)}_{Quartz,PP,B}(\omega) = -L_{XX}(\omega)L_{YY}(\omega_1)L_{YY}(\omega_1)\cos\alpha_a\cos\alpha_a\cos\alpha_a\beta^{(2)}_{xxx}\cos3\varphi_a \quad (6)$$

where $L_{II}(\omega)$s are local field factors (*II*=XX or YY), α_a are incident and reflection angles for the the fundamental light and the *b*-ESHG light, $\beta^{(2)}_{xxx}$ is achiral hyperpolarizabilty for the α-quartz crystals, and φ_a azimuthal angle (0° is defined to be along the +X axis). The effective bulk macroscopic susceptibility for the α-quartz crystals along the +X axis is dominated by bulk, as expressed as $\chi^{(2)}_{\mathrm{Quartz,eff}}(\omega) \approx \frac{\chi^{(2)}_{\mathrm{Quartz,B}}(\omega)}{-i\Delta k_z} = ia\beta^{(2)}_{xxx}$, where a>0 for S-in/P-out, and a<0 for P-in/P-out with all L_{II} greater than 0. Thus, these spectral phases are dependent on the polarization combinations measured. Recently, Wang and coworkers set forth a SFG convention to calibrate

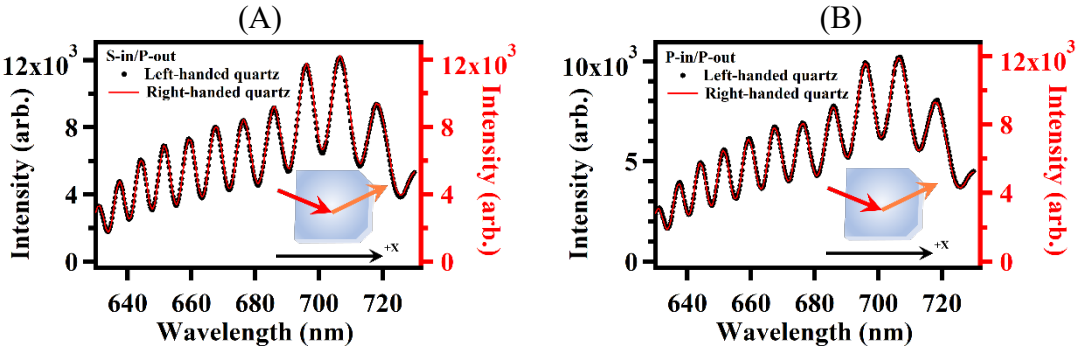

Figure 2. Interference *b*-ESHG spectra for left-handed and right-handed z-cut α-quartz crystals along the +X axis, with a local oscillator of z-cut quartz, for S-in/P-out (A), and P-in/P-out (B).

the absolute phase of the hyperpolarizability for α-quartz crystal.[73] It was found that the $\beta^{(2)}_{xxx}$, for left-handed and right-handed α-quartz crystals possess the same negative sign, namely, $\beta^{(2)}_{xxx}$ <0. Thus, the absolute phases of $\chi^{(2)}_{Quartz,B}$ for S-in/P-out and P-in/P-out were found to be -90° and 90°, respectively for both the left-handed and right-handed z-cut α-quartz crystals.

Absolute phases of $\chi^{(2)}$ for Au and Ag thin films. Au and Ag thin films are often used for calibration and as phase references in SFG experiments. Previous efforts were made to use adsorbates on Au and Ag surfaces in order to deduce their phases from either fittings or known responses of chemical groups.[57, 87-92] More importantly, these phases from VSFG are only for a small range of wavelength. As such, it is desirable to measure phases of Au and Ag over a broad

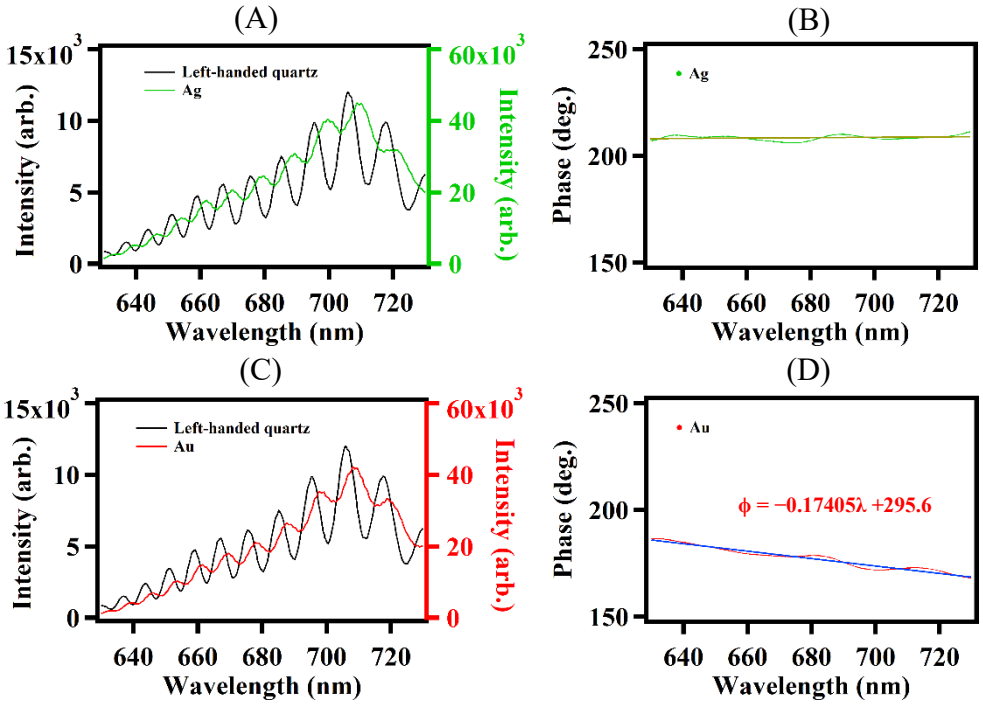

Figure 3. Interference *b*-ESHG spectra of P-in/P-out polarization for Ag thin films (A), and Au thin films (C). The left-handed z-cut α-quartz crystal along the +X direction was used as a reference. The spectral phases extracted as a function of wavelength for Ag thin films (B), and Au thin film (D).

range of wavelength to validate them as standard phase references in interfacial electronic spectroscopy.

Both the Au and Ag thin films produce stronger SHG intensities for P-in/P-out than those for other polarization combinations. Figure 3 shows interference *b*-SHG spectra for both silver (A) and gold (C) thin films for P-in/P-out polarization combination. Both the Au and Ag thin films

exhibit significant phase shifts with respect to that of the left-handed z-cut α-quartz crystal. The phases of Ag were independent of wavelength from 630 nm to 730 nm, as displayed in Figure 3 (B). Since the left-handed Z-cut quartz was oriented in the +X axis with a phase of 90° for P-in/P-out polarization as derived in Equation 6, the absolute phase of $\chi^{(2)}$ for the Ag thin films was found to be 210.0 ± 6.0°. Although Ag has a plasmonic resonance wavelength of 400 nm away from the ESHG and fundamental light wavelengths, ESHG responses of Ag thin films come from both the bulk and the surface. The surface contributions could not be simply neglected, unlike in the left-handed and right-handed z-cut α-quartz crystals. The phases of $\chi^{(2)}_{\text{eff}}$ are determined by both bulk susceptibility, $\chi^{(2)}_{\text{Bulk}}$, and surface susceptibility, $\chi^{(2)}_{\text{Surface}}$. The former is 90° shift from that for the latter. As a result, the phases of Ag thin films are different from those for the quartz, even though the phases are independent of frequency. On the other hand, the phases of $\chi^{(2)}$ for the Au thin films decrease from +187.0 ± 6.0° to +168.0 ± 6.0° from 630 nm to 730 nm, as shown in Figure 3 (D). We have fitted the phases as a function of wavelength for Au thin films, with an equation of $\phi(\lambda) = 0.17405\lambda + 295.6$ (λ: nm). In addition, we have obtained the frequency-dependent phases for Au thin films with $\phi(\nu) = 42.458\,\nu + 59.332$ (ν: rad/fs), as shown in Figure S3. The frequency-dependent phases of Au thin films are related to the metal electronic properties. For the Ag thin films, the *d*-band is comparatively far in energy from the fundamental and SHG wavelengths in our experiments. For the Au thin films, photoexcited electrons were nearly resonant with those transitions from *d*- to *s*-bands near 530 nm, being close to our SHG wavelengths. As such, Au thin films could not be used as a phase standard in this wavelength range, while Ag thin films are an excellent choice as a phase standard used from 600 nm to 730 nm.

Absolute phase of $\chi^{(2)}$ for p-type GaP (100). Historically, GaP was used as a standard to examine the sign of the hyperpolarizability, $\beta^{(2)}$, for quartz crystals.[73, 93] We chose *p*-type GaP (100) as a reference since it is transparent to both the fundamental wavelength (1200 - 1500 nm) and the second harmonic wavelength (600 - 750 nm). Figure 4 (A) presents interference *b*-ESHG spectra (P-in/P-out) for *p*-type GaP (100) along the $[01\bar{1}]$ direction. The interference spectrum for the GaP exhibits a same sign along the direction as compared with that for the left-handed z-cut α-quartz crystal along the +X direction. Figure 4(B) shows that the phases for *p*-type GaP (100) along the $[01\bar{1}]$ direction were independent of wavelength from 630 nm to 730 nm. The absolute phase of

the GaP (100) along the [01$\bar{1}$] direction was found to be 92.0 ± 6°. Thus, GaP is also a good option for standard phase of second-order electronic spectroscopy.

We further examined the sign of $\beta^{(2)}$ for GaP (100). The GaP crystal exhibits a zinc blende structure $\bar{4}$3m (T_d). Along the [011] and [01$\bar{1}$] directions, the macroscopic susceptibilities, $\chi^{(2)}_{GaP}$, are dominated by bulk. Thus, the macroscopic susceptibilities for S-in/P-out and P-in/P-out for GaP (100) are generally expressed as[7, 35]

$$\chi^{(2)}_{GaP,SP,B} = L_{ZZ}(\omega)L_{YY}(\omega_1)L_{YY}(\omega_1)\sin\alpha_b\,\beta^{(2)}_{abc,B}\cos2\varphi_b$$

$$\begin{aligned}\chi^{(2)}_{GaP,PP,B} = &-L_{XX}(\omega)L_{XX}(\omega_1)L_{ZZ}(\omega_1)\cos\alpha_b\cos\alpha_b\sin\alpha_b\,\beta^{(2)}_{abc,B}\cos2\varphi_b\\ &-L_{XX}(\omega)L_{ZZ}(\omega_1)L_{XX}(\omega_1)\cos\alpha_b\sin\alpha_b\cos\alpha_b\,\beta^{(2)}_{abc,B}\cos2\varphi_b\\ &+L_{ZZ}(\omega)L_{XX}(\omega_1)L_{XX}(\omega_1)\sin\alpha_b\cos\alpha_b\cos\alpha_b\,\beta^{(2)}_{abc,B}\cos2\varphi_b\end{aligned} \quad (7)$$

where φ_b is the azimuthal angle, φ_b= 0° is defined to be along the [011] axis, φ_b= 90° along the [01$\bar{1}$] axis, α_b the incident and reflection angles for the fundamental and the *b*-ESHG light, $\beta^{(2)}_{abc,B}$ is the bulk dipole-allowed hyperpolarizability for GaP. The effective bulk macroscopic susceptibilities for GaP (001) along the [01$\bar{1}$] direction (φ_b= 90°) is dominated by bulk, as expressed as $\frac{\chi^{(2)}_{GaP,B}(\omega)}{-i\Delta k_z} \approx ib\beta^{(2)}_{abc,B}$, where *b*<0 for S-in/P-out and *b*>0 for P-in/P-out with all the local field factor *L*s are greater than 0. It was found from Figure 4 (B) that the phases for the *p*-type GaP (100) along the [01$\bar{1}$] axis were the same as that for the left-handed z-cut α-quartz crystal

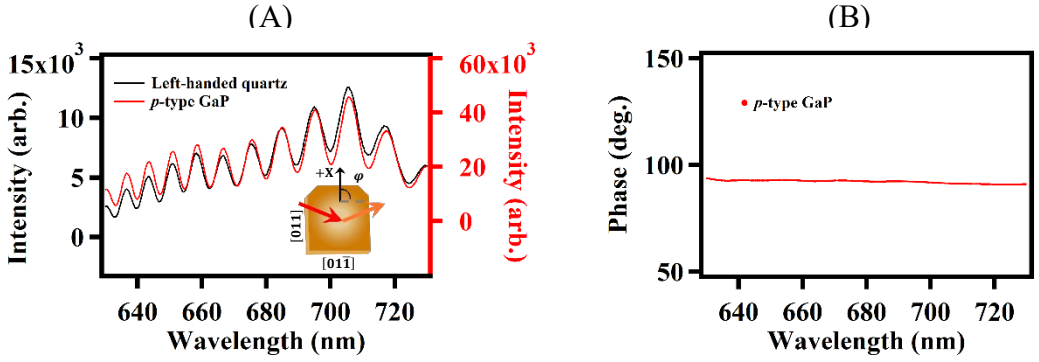

Figure 4. (A) Interference *b*-ESHG spectra (P-in/P-out) from *p*-type GaP (100) along the [01$\bar{1}$] as compared with that for the left-handed z-cut α-quartz crystal along the +X axis. (B) The extracted absolute phase along the [01$\bar{1}$] direction of *p*-type GaP (100) as a function of wavelength.

along the +X axis in P-in/P-out, being the absolute value close to 90°. Thus, $\beta^{(2)}_{\mathrm{abc,B}}$ was determined to be positive, which is consistent with that reported in the literature.[93]

Absolute phases of $\chi^{(2)}$ for p-type GaAs (100) with Azimuthal Angles. GaAs exhibits high second-order nonlinear optical responses, thereby being a routine reference for SFG experiments.[35] However, the spectral phases of second order susceptibility for GaAs are not well known. In addition, anisotropic crystals have distinct phases along different crystal axes. To understand spectral phases of anisotropic GaAs crystals, we collected interference *b*-ESHG spectra as a function of azimuthal angle. Figure 5 (A) shows pseudo-color 2D plot of interference *b*-ESHG spectra (P-in/P-out) from *p*-type GaAs (100) as a function of azimuthal angle. Here, 0° is defined to be along the [011] axis and 90° along the $[01\bar{1}]$ axis. Figure 5 (B) presents ESHG intensities as a function of azimuthal angle along the [011] and $[01\bar{1}]$ at the representative wavelengths of 653 nm and 694 nm. The angle-dependent SHG intensities of the GaAs crystal are consistent with those reported in the literature.[35, 79, 94] Both the *p*-type GaAs (100) and the *p*-type GaP (100) exhibit the same structure of a zinc blende $\bar{4}3\mathrm{m}$ ($\mathrm{T_d}$). As such, Equation 7 also applies to the case for GaAs. The effective macroscopic susceptibilities for the *p*-type GaAs (100) along the directions of [011] and $[01\bar{1}]$ are dominated by bulk, as expressed as $\frac{\chi^{(2)}_{GaAs,B}(\omega)}{-i\Delta k_z}$. We compared the spectral phases for the GaAs to that for the left-handed z-cut α-quartz crystal along the +X axis. Figure 5 (C) displays extracted absolute phases as a function of azimuthal angle at 650 nm and 700 nm as two representatives. The spectral phases show sharp change near 45°, 135°, 225°, and 315°. These well-patterned phases are due to the azimuth-dependent susceptibilities as shown in Equation 7. Figure 5 (D) shows absolute phases with wavelength along the [011] and $[01\bar{1}]$. The spectral phases along the two axes are flat and independent of wavelength. It was found that the spectral phases alternately occur at -103.0 ± 6.0° and 68.0 ± 6.0° with the azimuthal angle. These values of phases for the GaAs along the [011] and $[01\bar{1}]$ deviate from -90° and +90°. The GaAs crystal possesses a band gap of ca. 870 nm. The SHG wavelengths from 630 nm to 730 nm fall in the region of transitions from lower valleys to higher valleys in the GaAs.[85, 95, 96] These dispersions are likely responsible for the phase deviations above.

Discussion

Absolute phase of $\chi^{(2)}(\omega)$ for a reference is crucial for further determination of spectral phases for other unknown samples. Absolute spectral phases of $\chi^{(2)}(\omega)$ for three kinds of reference materials, including insulators (left-handed and right-handed α-quartz crystals), semiconductors (*p*-type GaP (100) and GaAs (100)), and metallic films (Au and Ag thin films), have been examined in our HD-iES experiments. The determination of absolute phases of $\chi^{(2)}(\omega)$ is sensitive to measured polarization as well as crystal orientations for anisotropic materials. The phases for both the left-handed and right-handed α-quartz crystals are found to be -90° and 90° in S-in/P-out and P-in/P-out polarization combinations, respectively. The phases of the α-quartz crystals are wavelength-independent since they are transparent in the wavelength window from

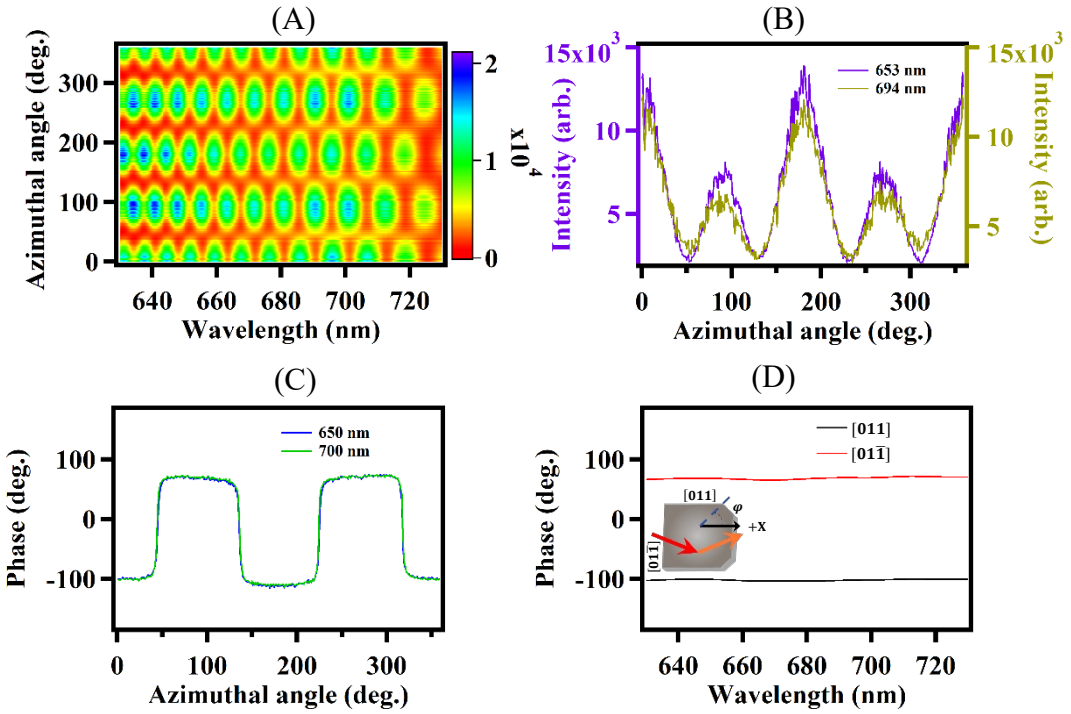

Figure 5. (A) Pseduo-color 2D plot of interference *b*-ESHG spectra (P-in/P-out) from *p*-type GaAs (100) as a function of azimuthal angle. (B) *b*-ESHG intensities as a function of azimuthal angle along the [011] and [01$\bar{1}$] at 653 nm and 694 nm. (C) Absolute phases extracted as a function of azimuthal angle at 650 nm and 700 nm. (D) Wavelength-dependent absolute phases along the [011] and [01$\bar{1}$].

550 nm to 1800 nm. The *p*-type GaP (100) crystal along the the [01$\bar{1}$] direction exhibits the wavelength-independent spectral phase of 92 ± 6.0° similar to the α-quartz crystals for P-in/P-out measurements. As expected, the GaP materials are also transparent to the wavelength window of interest. As such, both the α-quartz crystals and GaP crystals are good choices for phase references. Ag thin films show wavelength-independent spectral phases of $\chi^{(2)}(\omega)$ with a value of 210.0 ±

6.0° and are the best choice for phase references. On the other hand, Au thin films are often used for a phase reference in the literature but exhibit wavelength-dependent spectral phases of $\chi^{(2)}(\omega)$. Here, a guideline for a phase reference is suggested to make reference to the frequencies of light employed by VSFG and ESFG/ESHG. A. Consideration of polarization combinations. Absolute phases for references depend on polarization combinations applied in VSFG or ESFG/ESHG. For example, the absolute phases for S-in/P-out and P-in/P-out in ESHG were found to be -90° and 90°, respectively for both the left-handed and right-handed z-cut α-quartz crystals. B. Choices of references: 1) Z-cut left-handed/right-handed α-quartz crystals are the best choices as a phase reference for all ESFG/ESHG involved lights from 200 –2000 nm, but only good in the IR range of 4000 – 2500 cm^{-1} for VSFG. 2) Ag thin films are always the best choices as a phase reference for VSFG in the IR range of 4000 – 1000 cm^{-1} with a visible beam's wavelength longer than 530 nm, and for all ESFG/ESHG involved lights longer than 450 nm. The absolute phases for Ag thin films, independent of wavelength, are different from those for Z-cut left-handed/right-handed α-quartz crystals. 3) Au thin films are suggested not to be used as a phase reference for either ESFG or VSFG since their absolute phases are wavelength-dependent from UV to visible range. 4) GaP(100) is limited to VSFG and ESFG/ESHG of all involved lights from 600 nm to IR. The absolute phases for GaP depend on crystal orientations. Crystal orientations needs to be calibrated. 5) GaAs(100) is limited to VSFG and ESFG/ESHG of all involved lights from 950 nm to IR. The absolute phases for GaAs depend on crystal orientations. Crystal orientations needs to be calibrated.

It is noted that phase accuracy is an important criterion for further applications of a phase method. For an electronic transition with a typical damping rate of 500 cm^{-1}, one spectral interference cycle could cover 100-500 cm^{-1}. The more points a spectral interference cycle spans, the better a phase resolution. On the other hand, the time delay between the "DC" and the "AC" in the HD method is only 100 fs when the cycle goes beyond 330 cm^{-1}. Such a short delay leads to a challenge for Fourier filtering. Considering both the time delay and the phase resolution, each cycle with 42 data points gives rise to a phase resolution of 11° in our HD-iES (a time delay generator of 3mm). Based on our experiments, the phase accuracy was on the order of 6°. Likewise, one could estimate phase accuracy for heterodyne vibrational SFG (HD-VSFG). For a vibrational peak with a typical damping rate of 15 cm^{-1}, one interference cycle covers the entire vibrational peak with a cycle of 30 cm^{-1}. A time delay of 1.1 ps is required to generate the spectral interference cycle of 30 cm^{-1}. To achieve a phase resolution of 5° in the HD-VSFG, each data point spans ca.

0.4 cm^{-1}. Thus, one should consider an appropriate spectrometer and CCD in HD-VSFG for fine spectral resolution. In the case of a high resolution VSFG for heterodyne detection, a well-designed detection system is needed for HD measurements.

Conclusions

In summary, we have presented an easy-to-implement heterodyne detection of interfacial broadband electronic spectroscopy (HD-iES) for spectral phase measurements. The HD method provided a broad spectral range from 550 nm to 1100 nm with a short-wave IR laser source of 1100-2200 nm. High phase stability has been maintained due to the collinear geometry. In our case a phase error of 6° was achieved. We further examined spectral absolute phases for six references, including left-handed α-quartz crystals, right-handed α-quartz crystals, Au thin films, Ag thin films, *p*-type GaP (100), and *p*-type GaAs (100). In addition to the left-handed and right-handed α-quartz crystals, the Ag thin films, GaP, and GaAs crystals are also good choices for phase references with frequency-independent phases in HD-iES. On the other hand, Au thin films with frequency-dependent phases are not good phase references, even though they are often used in the literature. These results extend more applications of phase measurements into interfacial electronic spectroscopy.

Supporting Information

The supporting information contains Calculations of $\chi_{eff}^{(2)}$ for Ag, Au, GaP(100), and GaAs(100). The following supporting figures are provided in the supporting information: SFG cross correlation measurements by mixing an 800 nm (100 fs) with the SWIR pulse, Figure S1; AFM AFM Characterization of thickness of Au thin films, Figure S2; The spectral phases extracted as a function of frequency for Ag thin films (A), and Au thin films (B), Figure S3.

Acknowledgments

This material is based upon work supported by the National Science Foundation under Grant No. [2045084]. Y.R. is also grateful for Utah State University for the generous start-up fund. Z.L. is grateful for the financial support from the National Science Foundation of China (Grant No. 22073001). The authors thank Dr. Hongfei Wang in Westlake University and Mr. Hui Wang in Fudan University for calibrating quartz crystals with vibrational SFG.

References

(1) Shen, Y. R. Surface Properties Probed by Second-Harmonic and Sum-Frequency Generation. *Nature* **1989**, *337*, 519-525.
(2) Eisenthal, K. B. Photochemistry and Photophysics of Liquid Interfaces by Second Harmonic Spectroscopy. *J. Phys. Chem.* **1996**, *100*, 12997-13006.
(3) Eisenthal, K. B. Liquid Interfaces Probed by Second-Harmonic and Sum-Frequency Spectroscopy. *Chem. Rev.* **1996**, *96*, 1343-1360.
(4) Miranda, P. B.; Shen, Y. R. Liquid Interfaces: A Study by Sum-Frequency Vibrational Spectroscopy. *J. Phys. Chem. B* **1999**, *103*, 3292-3307.
(5) Chen, Z.; Shen, Y.; Somorjai, G. A. Studies of Polymer Surfaces by Sum Frequency Generation Vibrational Spectroscopy. *Annu. Rev. Phys. Chem.* **2002**, *53*, 437-465.
(6) Richmond, G. L. Molecular Bonding and Interactions at Aqueous Surfaces as Probed by Vibrational Sum Frequency Spectroscopy. *Chem. Rev.* **2002**, *102*, 2693-2724.
(7) Wang, H. F.; Gan, W.; Lu, R.; Rao, Y.; Wu, B. H. Quantitative Spectral and Orientational Analysis in Surface Sum Frequency Generation Vibrational Spectroscopy (SFG-VS). *Int. Rev. Phys. Chem.* **2005**, *24*, 191-256.
(8) Geiger, F. M. Second Harmonic Generation, Sum Frequency Generation, and $X^{(3)}$: Dissecting Environmental Interfaces with a Nonlinear Optical Swiss Army Knife. *Annu. Rev. Phys. Chem.* **2009**, *60*, 61-83.
(9) Arnolds, H.; Bonn, M. Ultrafast Surface Vibrational Dynamics. *Surf. Sci. Rep.* **2010**, *65*, 45-66.
(10) Jubb, A. M.; Hua, W.; Allen, H. C. Environmental Chemistry at Vapor/Water Interfaces: Insights from Vibrational Sum Frequency Generation Spectroscopy. *Annu. Rev. Phys. Chem.* **2012**, *63*, 107-130.
(11) Johnson, C. M.; Baldelli, S. Vibrational Sum Frequency Spectroscopy Studies of the Influence of Solutes and Phospholipids at Vapor/Water Interfaces Relevant to Biological and Environmental Systems. *Chem. Rev.* **2014**, *114*, 8416-8446.
(12) Yan, E. C. Y.; Fu, L.; Wang, Z. G.; Liu, W. Biological Macromolecules at Interfaces Probed by Chiral Vibrational Sum Frequency Generation Spectroscopy. *Chem. Rev.* **2014**, *114*, 8471-8498.
(13) Berne, B. J.; Fourkas, J. T.; Walker, R. A.; Weeks, J. D. Nitriles at Silica Interfaces Resemble Supported Lipid Bilayers. *Acc. Chem. Res.* **2016**, *49*, 1605-1613.
(14) Kung, K. Y.; Chen, P.; Wei, F.; Shen, Y. R.; Somorjai, G. A. Sum-Frequency Generation Spectroscopic Study of Co Adsorption and Dissociation on Pt(111) at High Pressure and Temperature. *Surf. Sci.* **2000**, *463*, L627-L633.
(15) Wang, C. Y.; Groenzin, H.; Shultz, M. J. Surface Characterization of Nanoscale TiO_2 Film by Sum Frequency Generation Using Methanol as a Molecular Probe. *J. Phys. Chem. B* **2004**, *108*, 265-272.
(16) Rao, Y.; Song, D.; Turro, N. J.; Eisenthal, K. B. Orientational Motions of Vibrational Chromophores in Molecules at the Air/Water Interface with Time-Resolved Sum Frequency Generation. *J. Phys. Chem. B* **2008**, *112*, 13572-13576.
(17) Sekiguchi, K.; Yamaguchi, S.; Tahara, T. Femtosecond Time-Resolved Electronic Sum-Frequency Generation Spectroscopy: A New Method to Investigate Ultrafast Dynamics at Liquid Interfaces. *J. Chem. Phys.* **2008**, *128*, 114715.

(18) Anglin, T. C.; Conboy, J. C. Kinetics and Thermodynamics of Flip-Flop in Binary Phospholipid Membranes Measured by Sum-Frequency Vibrational Spectroscopy. *Biochemistry* **2009**, *48*, 10220-10234.
(19) Rao, Y.; Turro, N. J.; Eisenthal, K. B. Solvation Dynamics at the Air/Water Interface with Time-Resolved Sum-Frequency Generation. *J. Phys. Chem. C* **2010**, *114*, 17703-17708.
(20) Yamamoto, S.; Ghosh, A.; Nienhuys, H.-K.; Bonn, M. Ultrafast Inter- and Intramolecular Vibrational Energy Transfer between Molecules at Interfaces Studied by Time- and Polarization-Resolved SFG Spectroscopy. *Phys. Chem. Chem. Phys.* **2010**, *12*, 12909-12918.
(21) Stiopkin, I. V.; Weeraman, C.; Pieniazek, P. A.; Shalhout, F. Y.; Skinner, J. L.; Benderskii, A. V. Hydrogen Bonding at the Water Surface Revealed by Isotopic Dilution Spectroscopy. *Nature* **2011**, *474*, 192-195.
(22) Rao, Y.; Hong, S.-Y.; Turro, N. J.; Eisenthal, K. B. Molecular Orientational Distribution at Interfaces Using Second Harmonic Generation. *J. Phys. Chem. C* **2011**, *115*, 11678-11683.
(23) Laaser, J. E.; Xiong, W.; Zanni, M. T. Time-Domain SFG Spectroscopy Using Mid-IR Pulse Shaping: Practical and Intrinsic Advantages. *J. Phys. Chem. B* **2011**, *115*, 2536-2546.
(24) Rao, Y.; Xu, M.; Jockusch, S.; Turro, N. J.; Eisenthal, K. B. Dynamics of Excited State Electron Transfer at a Liquid Interface Using Time-Resolved Sum Frequency Generation. *Chem. Phys. Lett.* **2012**, *544*, 1-6.
(25) Liljeblad, J. F.; Tyrode, E. Vibrational Sum Frequency Spectroscopy Studies at Solid/Liquid Interfaces: Influence of the Experimental Geometry in the Spectral Shape and Enhancement. *J. Phys. Chem. C* **2012**, *116*, 22893-22903.
(26) Laaser, J. E.; Zanni, M. T. Extracting Structural Information from the Polarization Dependence of One- and Two-Dimensional Sum Frequency Generation Spectra. *J. Phys. Chem. A* **2013**, *117*, 5875-5890.
(27) Wen, Y.-C.; Zha, S.; Liu, X.; Yang, S.; Guo, P.; Shi, G.; Fang, H.; Shen, Y. R.; Tian, C. Unveiling Microscopic Structures of Charged Water Interfaces by Surface-Specific Vibrational Spectroscopy. *Phys. Rev. Lett.* **2016**, *116*, 016101.
(28) Deng, G. H.; Li, X.; Liu, S. L.; Zhang, Z.; Lu, Z.; Guo, Y. Successive Adsorption of Cations and Anions of Water-1-Butyl-3-Methylimidazolium Methylsulfate Binary Mixtures at the Air-Liquid Interface Studied by Sum Frequency Generation Vibrational Spectroscopy and Surface Tension Measurements. *J. Phys. Chem. C* **2016**, *120*, 12032-12041.
(29) Xiang, B.; Li, Y.; Pham, C. H.; Paesani, F.; Xiong, W. Ultrafast Direct Electron Transfer at Organic Semiconductor and Metal Interfaces. *Sci. Adv.* **2017**, *3*, e1701508.
(30) Vanselous, H.; Stingel, A. M.; Petersen, P. B. Interferometric 2D Sum Frequency Generation Spectroscopy Reveals Structural Heterogeneity of Catalytic Monolayers on Transparent Materials. *J. Phys. Chem. Lett.* **2017**, *8*, 825-830.
(31) Elsenbeck, D.; Das, S. K.; Velarde, L. Substrate Influence on the Interlayer Electron–Phonon Couplings in Fullerene Films Probed with Doubly-Resonant SFG Spectroscopy. *Phys. Chem. Chem. Phys.* **2017**, *19*, 18519-18528.
(32) Rey, N. G.; Dlott, D. D. Studies of Electrochemical Interfaces by Broadband Sum Frequency Generation. *J. Electroanal. Chem.* **2017**, *800*, 114-125.
(33) Ma, Y.; Xie, Y.; Lin, L.; Zhang, L.; Liu, M.; Guo, Y.; Lan, Z.; Lu, Z. Photodimerization Kinetics of a Styrylquinoline Derivative in Langmuir–Blodgett Monolayers Monitored by Second Harmonic Generation. *J. Phys. Chem. C* **2017**, *121*, 23541-23550.

(34) Feng, R.-J.; Lin, L.; Li, Y.-Y.; Liu, M.-H.; Guo, Y.; Zhang, Z. Effect of Ca^{2+} to Sphingomyelin Investigated by Sum Frequency Generation Vibrational Spectroscopy. *Biophys. J.* **2017**, *112*, 2173-2183.
(35) Zhang, Z.; Kim, J.; Khoury, R.; Saghayezhian, M.; Haber, L. H.; Plummer, E. Surface Sum Frequency Generation Spectroscopy on Non-Centrosymmetric Crystal GaAs (001). *Surf. Sci.* **2017**, *664*, 21-28.
(36) Tan, J.; Zhang, B.; Luo, Y.; Ye, S. Ultrafast Vibrational Dynamics of Membrane-Bound Peptides at the Lipid Bilayer/Water Interface. *Angew. Chem., Int. Ed.* **2017**, *56*, 12977-12981.
(37) Chowdhury, A. U.; Liu, F.; Watson, B. R.; Ashkar, R.; Katsaras, J.; Patrick Collier, C.; Lutterman, D. A.; Ma, Y.-Z.; Calhoun, T. R.; Doughty, B. Flexible Approach to Vibrational Sum-Frequency Generation Using Shaped near-Infrared Light. *Opt. Lett.* **2018**, *43*, 2038-2041.
(38) DelloStritto, M.; Piontek, S. M.; Klein, M. L.; Borguet, E. Relating Interfacial Order to Sum Frequency Generation with Ab Initio Simulations of the Aqueous $Al_2O_3(0001)$ and $(11\bar{2}0)$ Interfaces. *J. Phys. Chem. C* **2018**, *122*, 21284-21294.
(39) Watson, B. R.; Doughty, B.; Calhoun, T. R. Energetics at the Surface: Direct Optical Mapping of Core and Surface Electronic Structure in Cdse Quantum Dots Using Broadband Electronic Sum Frequency Generation Microspectroscopy. *Nano Lett.* **2019**, *19*, 6157-6165.
(40) Rao, Y.; Qian, Y.; Deng, G.-H.; Kinross, A.; Turro, N. J.; Eisenthal, K. B. Molecular Rotation in 3 Dimensions at an Air/Water Interface Using Femtosecond Time Resolved Sum Frequency Generation. *J. Chem. Phys.* **2019**, *150*, 094709.
(41) Raab, M.; Becca, J. C.; Heo, J.; Lim, C. K.; Baev, A.; Jensen, L.; Prasad, P. N.; Velarde, L. Doubly Resonant Sum Frequency Spectroscopy of Mixed Photochromic Isomers on Surfaces Reveals Conformation-Specific Vibronic Effects. *J. Chem. Phys.* **2019**, *150*, 114704.
(42) Liu, Z.; Li, Y.; Xu, Q.; Wang, H.; Liu, W.-T. Coherent Vibrational Spectroscopy of Electrochemical Interfaces with Plasmonic Nanogratings. *J. Phys. Chem. Lett.* **2020**, *11*, 243-248.
(43) Deng, G.-H.; Qian, Y.; Wei, Q.; Zhang, T.; Rao, Y. Interface-Specific Two-Dimensional Electronic Sum Frequency Generation Spectroscopy. *J. Phys. Chem. Lett.* **2020**, *11*, 1738-1745.
(44) Superfine, R.; Huang, J. Y.; Shen, Y. R. Experimental Determination of the Sign of Molecular Dipole Moment Derivatives: An Infrared—Visible Sum Frequency Generation Absolute Phase Measurement Study. *Chem. Phys. Lett.* **1990**, *172*, 303-306.
(45) Yamaguchi, S.; Tahara, T. Heterodyne-Detected Electronic Sum Frequency Generation: "Up" Versus "Down" Alignment of Interfacial Molecules. *J. Chem. Phys.* **2008**, *129*, 101102.
(46) Thämer, M.; Garling, T.; Campen, R. K.; Wolf, M. Quantitative Determination of the Nonlinear Bulk and Surface Response from Alpha-Quartz Using Phase Sensitive SFG Spectroscopy. *J. Chem. Phys.* **2019**, *151*, 064707.
(47) Moon, A. P.; Pandey, R.; Bender, J. A.; Cotton, D. E.; Renard, B. A.; Roberts, S. T. Using Heterodyne-Detected Electronic Sum Frequency Generation to Probe the Electronic Structure of Buried Interfaces. *J. Phys. Chem. C* **2017**, *121*, 18653-18664.
(48) Ohno, P. E.; Saslow, S. A.; Wang, H.-f.; Geiger, F. M.; Eisenthal, K. B. Phase-Referenced Nonlinear Spectroscopy of the α-Quartz/Water Interface. *Nat. Commun.* **2016**, *7*, 13587.
(49) Rich, C. C.; Lindberg, K. A.; Krummel, A. T. Phase Acrobatics: The Influence of Excitonic Resonance and Gold Nonresonant Background on Heterodyne-Detected Vibrational Sum Frequency Generation Emission. *J. Phys. Chem. Lett.* **2017**, *8*, 1331-1337.
(50) Superfine, R.; Huang, J. Y.; Shen, Y. R. Phase Measurement for Surface Infrared–Visible Sum-Frequency Generation. *Opt. Lett.* **1990**, *15*, 1276-1278.

(51) Stiopkin, I. V.; Jayathilake, H. D.; Bordenyuk, A. N.; Benderskii, A. V. Heterodyne-Detected Vibrational Sum Frequency Generation Spectroscopy. *J. Am. Chem. Soc.* **2008**, *130*, 2271-2275.
(52) Yamaguchi, S.; Otosu, T. Progress in Phase-Sensitive Sum Frequency Generation Spectroscopy. *Phys. Chem. Chem. Phys.* **2021**, *23*, 18253-18267.
(53) Farah, Y. R.; Krummel, A. T. The Ph-Dependent Orientation of N3 Dye on a Gold Substrate Is Revealed Using Heterodyne-Detected Vibrational Sum Frequency Generation Spectroscopy. *J. Chem. Phys.* **2021**, *154*, 124702.
(54) Roy, S.; Saha, S.; Mondal, J. A. In *Modern Techniques of Spectroscopy: Basics, Instrumentation, and Applications*; Singh, D. K., Pradhan, M., Materny, A. Eds.; Springer: Singapore, 2021; vol. 13, pp 87-115.
(55) Myalitsin, A.; Ghosh, S.; Urashima, S.-h.; Nihonyanagi, S.; Yamaguchi, S.; Aoki, T.; Tahara, T. Structure of Water and Polymer at the Buried Polymer/Water Interface Unveiled Using Heterodyne-Detected Vibrational Sum Frequency Generation. *Phys. Chem. Chem. Phys.* **2020**, *22*, 16527-16531.
(56) Saha, S.; Roy, S.; Mathi, P.; Mondal, J. A. Polyatomic Iodine Species at the Air–Water Interface and Its Relevance to Atmospheric Iodine Chemistry: An HD-VSFG and Raman-MCR Study. *J. Phys. Chem. A* **2019**, *123*, 2924-2934.
(57) Marmolejos, J. M.; Bisson, P. J.; Shultz, M. J. Gold as a Standard Phase Reference in Complex Sum Frequency Generation Measurements. *J. Chem. Phys.* **2019**, *150*, 124705.
(58) Wang, J.; Bisson, P. J.; Marmolejos, J. M.; Shultz, M. J. Nonlinear Interferometer: Design, Implementation, and Phase-Sensitive Sum Frequency Measurement. *J. Chem. Phys.* **2017**, *147*, 064201.
(59) Vanselous, H.; Petersen, P. B. Extending the Capabilities of Heterodyne-Detected Sum-Frequency Generation Spectroscopy: Probing Any Interface in Any Polarization Combination. *J. Phys. Chem. C* **2016**, *120*, 8175-8184.
(60) Rich, C. C.; Mattson, M. A.; Krummel, A. T. Direct Measurement of the Absolute Orientation of N3 Dye at Gold and Titanium Dioxide Surfaces with Heterodyne-Detected Vibrational SFG Spectroscopy. *J. Phys. Chem. C* **2016**, *120*, 6601-6611.
(61) Hu, D.; Chou, K. C. Surface Charge at the Bitumen/Water Interface Investigated by Phase-Sensitive Sum Frequency Generation Vibrational Spectroscopy: Effects of pH, Ions, and Surfactants. *Energy Fuels* **2015**, *29*, 7885-7888.
(62) Ge, A.; Peng, Q.; Qiao, L.; Yepuri, N. R.; Darwish, T. A.; Matsusaki, M.; Akashi, M.; Ye, S. Molecular Orientation of Organic Thin Films on Dielectric Solid Substrates: A Phase-Sensitive Vibrational Sfg Study. *Phys. Chem. Chem. Phys.* **2015**, *17*, 18072-18078.
(63) Okuno, M.; Ishibashi, T.-a. Chirality Discriminated by Heterodyne-Detected Vibrational Sum Frequency Generation. *J. Phys. Chem. Lett.* **2014**, *5*, 2874-2878.
(64) Verreault, D.; Hua, W.; Allen, H. C. From Conventional to Phase-Sensitive Vibrational Sum Frequency Generation Spectroscopy: Probing Water Organization at Aqueous Interfaces. *J. Phys. Chem. Lett.* **2012**, *3*, 3012-3028.
(65) Wang, H. Y.; Gao, T.; Xiong, W. Self-Phase-Stabilized Heterodyne Vibrational Sum Frequency Generation Microscopy. *ACS Photonics* **2017**, *4*, 1839-1845.
(66) Xu, B.; Wu, Y.; Sun, D.; Dai, H.-L.; Rao, Y. Stabilized Phase Detection of Heterodyne Sum Frequency Generation for Interfacial Studies. *Opt. Lett.* **2015**, *40*, 4472-4475.
(67) Han, Y.; Raghunathan, V.; Feng, R.-r.; Maekawa, H.; Chung, C.-Y.; Feng, Y.; Potma, E. O.; Ge, N.-H. Mapping Molecular Orientation with Phase Sensitive Vibrationally Resonant Sum-Frequency Generation Microscopy. *J. Phys. Chem. B* **2013**, *117*, 6149-6156.

(68) Kemnitz, K.; Bhattacharyya, K.; Hicks, J. M.; Pinto, G. R.; Eisenthal, B.; Heinz, T. F. The Phase of Second-Harmonic Light Generated at an Interface and Its Relation to Absolute Molecular Orientation. *Chem. Phys. Lett.* **1986**, *131*, 285-290.
(69) Ji, N.; Ostroverkhov, V.; Chen, C.-Y.; Shen, Y.-R. Phase-Sensitive Sum-Frequency Vibrational Spectroscopy and Its Application to Studies of Interfacial Alkyl Chains. *J. Am. Chem. Soc.* **2007**, *129*, 10056-10057.
(70) Shen, Y. R. Phase-Sensitive Sum-Frequency Spectroscopy. *Annu. Rev. Phys. Chem.* **2013**, *64*, 129-150.
(71) Covert, P. A.; FitzGerald, W. R.; Hore, D. K. Simultaneous Measurement of Magnitude and Phase in Interferometric Sum-Frequency Vibrational Spectroscopy. *J. Chem. Phys.* **2012**, *137*, 014201.
(72) Lu, R.; Rao, Y.; Zhang, W.; Wang, H.-f. Phase Measurement in Nonlinear Optics of Molecules at Air/Water Interface with Femtosecond Laser Pulses. *Proc. SPIE* **2002**, *4812*, 115-124.
(73) Hu, X.-H.; Wei, F.; Wang, H.; Wang, H.-F. α-Quartz Crystal as Absolute Intensity and Phase Standard in Sum-Frequency Generation Vibrational Spectroscopy. *J. Phys. Chem. C* **2019**, *123*, 15071-15086.
(74) Sun, S.; Bisson, P. J.; Bonn, M.; Shultz, M. J.; Backus, E. H. G. Phase-Sensitive Sum-Frequency Generation Measurements Using a Femtosecond Nonlinear Interferometer. *J. Phys. Chem. C* **2019**, *123*, 7266-7270.
(75) Yamaguchi, S.; Watanabe, H.; Mondal, S. K.; Kundu, A.; Tahara, T. "Up" Versus "Down" Alignment and Hydration Structures of Solutes at the Air/Water Interface Revealed by Heterodyne-Detected Electronic Sum Frequency Generation with Classical Molecular Dynamics Simulation. *J. Chem. Phys.* **2011**, *135*, 194705.
(76) Yamaguchi, S.; Kundu, A.; Sen, P.; Tahara, T. Communication: Quantitative Estimate of the Water Surface pH Using Heterodyne-Detected Electronic Sum Frequency Generation. *J. Chem. Phys.* **2012**, *137*, 151101.
(77) Mondal, S. K.; Inoue, K.-i.; Yamaguchi, S.; Tahara, T. Anomalous Effective Polarity of an Air/Liquid-Mixture Interface: A Heterodyne-Detected Electronic and Vibrational Sum Frequency Generation Study. *Phys. Chem. Chem. Phys.* **2015**, *17*, 23720-23723.
(78) Dorrer, C.; Belabas, N.; Likforman, J. P.; Joffre, M. Experimental Implementation of Fourier-Transform Spectral Interferometry and Its Application to the Study of Spectrometers. *Appl. Phys. B* **2000**, *70*, S99-S107.
(79) Nelson, C.; Luo, J.; Jen, A.-Y.; Laghumavarapu, R.; Huffaker, D.; Zhu, X.-Y. Time-, Energy-, and Phase-Resolved Second-Harmonic Generation at Semiconductor Interfaces. *J. Phys. Chem. C* **2014**, *118*, 27981-27988.
(80) Nowakowski, P. J.; Woods, D. A.; Bain, C. D.; Verlet, J. R. R. Time-Resolved Phase-Sensitive Second Harmonic Generation Spectroscopy. *J. Chem. Phys.* **2015**, *142*, 084201.
(81) Wilson, P. T.; Jiang, Y.; Aktsipetrov, O. A.; Mishina, E. D.; Downer, M. C. Frequency-Domain Interferometric Second-Harmonic Spectroscopy. *Opt. Lett.* **1999**, *24*, 496-498.
(82) Xu, P.; Huang, A.; Suntivich, J. Phase-Sensitive Second-Harmonic Generation of Electrochemical Interfaces. *J. Phys. Chem. Lett.* **2020**, *11*, 8216-8221.
(83) Ohno, P. E.; Chang, H.; Spencer, A. P.; Liu, Y.; Boamah, M. D.; Wang, H.-f.; Geiger, F. M. Beyond the Gouy–Chapman Model with Heterodyne-Detected Second Harmonic Generation. *J. Phys. Chem. Lett.* **2019**, *10*, 2328-2334.

(84) Shen, Y. R. Optical Second Harmonic Generation at Interfaces. *Annu. Rev. Phys. Chem.* **1989**, *40*, 327-350.
(85) Deng, G.-H.; Qian, Y.; Rao, Y. Development of Ultrafast Broadband Electronic Sum Frequency Generation for Charge Dynamics at Surfaces and Interfaces. *J. Chem. Phys.* **2019**, *150*, 024708.
(86) Deng, G.-H.; Wei, Q.; Qian, Y.; Zhang, T.; Leng, X.; Rao, Y. Development of Interface-/Surface-Specific Two-Dimensional Electronic Spectroscopy. *Rev. Sci. Instrum.* **2021**, *92*, 023104.
(87) Covert, P. A.; Hore, D. K. Assessing the Gold Standard: The Complex Vibrational Nonlinear Susceptibility of Metals. *J. Phys. Chem. C* **2015**, *119*, 271-276.
(88) Dreesen, L.; Humbert, C.; Celebi, M.; Lemaire, J. J.; Mani, A. A.; Thiry, P. A.; Peremans, A. Influence of the Metal Electronic Properties on the Sum-Frequency Generation Spectra of Dodecanethiol Self-Assembled Monolayers on Pt (111), Ag (111) and Au (111) Single Crystals. *Appl. Phys. B* **2002**, *74*, 621-625.
(89) Busson, B.; Dalstein, L. Nonlinear Optical Response of a Gold Surface in the Visible Range: A Study by Two-Color Sum-Frequency Generation Spectroscopy. III. Simulations of the Experimental SFG Intensities. *J. Chem. Phys.* **2018**, *149*, 154701.
(90) Dalstein, L.; Revel, A.; Humbert, C.; Busson, B. Nonlinear Optical Response of a Gold Surface in the Visible Range: A Study by Two-Color Sum-Frequency Generation Spectroscopy. I. Experimental Determination. *J. Chem. Phys.* **2018**, *148*, 134701.
(91) Busson, B.; Dalstein, L. Nonlinear Optical Response of a Gold Surface in the Visible Range: A Study by Two-Color Sum-Frequency Generation Spectroscopy. II. Model for Metal Nonlinear Susceptibility. *J. Chem. Phys.* **2018**, *149*, 034701.
(92) Lambert, A. G.; Davies, P. B.; Neivandt, D. J. Implementing the Theory of Sum Frequency Generation Vibrational Spectroscopy: A Tutorial Review. *Appl. Spectrosc. Rev.* **2005**, *40*, 103-145.
(93) Nelson, D. F.; Turner, E. H. Electro-Optic and Piezoelectric Coefficients and Refractive Index of Gallium Phosphide. *J. Appl. Phys.* **1968**, *39*, 3337-3343.
(94) Park, H.; Gutierrez, M.; Wu, X.; Kim, W.; Zhu, X.-Y. Optical Probe of Charge Separation at Organic/Inorganic Semiconductor Interfaces. *J. Phys. Chem. C* **2013**, *117*, 10974-10979.
(95) Spicer, W. E.; Liliental-Weber, Z.; Weber, E.; Newman, N.; Kendelewicz, T.; Cao, R.; McCants, C.; Mahowald, P.; Miyano, K.; Lindau, I. The Advanced Unified Defect Model for Schottky Barrier Formation. *J. Vac. Sci. Technol. B* **1988**, *6*, 1245-1251.
(96) Spicer, W. E.; Lindau, I.; Skeath, P.; Su, C. Y. Unified Defect Model and Beyond. *J. Vac. Sci. Technol.* **1980**, *17*, 1019-1027.

TOC Graphic

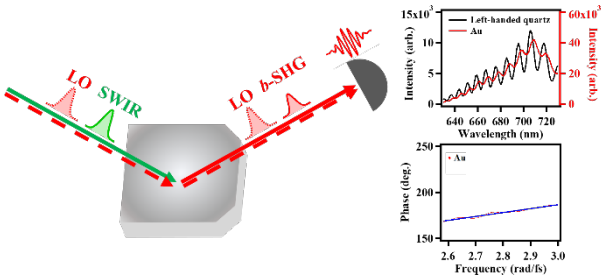
LO SWIR
LO b-SHG
15x10^3
10
5
0
Intensity (arb.)
Left-handed quartz
Au
60x10^3
40
20
0
Intensity (arb.)
640 660 680 700 720
Wavelength (nm)
250
200
150
Phase (deg.)
Au
2.6 2.7 2.8 2.9 3.0
Frequency (rad/fs)